

# Flexible circularly polarized antenna with axial ratio bandwidth enhancement for off-body communications

Hong Cai Yang<sup>1</sup>  | Xiong Ying Liu<sup>1,2</sup> | Yi Fan<sup>3</sup> | Manos M. Tentzeris<sup>4</sup>

<sup>1</sup>School of Electronic and Information Engineering, South China University of Technology, Guangzhou, China

<sup>2</sup>National Engineering Technology Research Center for Mobile Ultrasonic Detection, Guangzhou, China

<sup>3</sup>School of Electronics and Information, Guangdong Polytechnic Normal University, Guangzhou, China

<sup>4</sup>School of Electrical and Computer Engineering, Georgia Institute of Technology, Atlanta, USA

## Correspondence

Xiong Ying Liu, School of Electronic and Information Engineering, South China University of Technology, Guangzhou, People's Republic of China.  
Email: liuxy@scut.edu.cn

## Funding information

National Natural Science Foundation of China, Grant/Award Number: 61372008; Science and Technology Planning Project of Guangdong Province, Grant/Award Number: 2014A010103014, 2015B010101006; Foundation of the State Key Laboratory of Subtropical Building Science, Grant/Award Number: 2020ZA05

## Abstract

A flexible circularly polarized (CP) wearable antenna is proposed for a wireless body area network at the 5.8-GHz industrial, scientific, and medical band. The proposed antenna is made of flexible polyimide and foam material. The CP radiation is enabled by loading two pairs of shorting pins on a rectangular patch antenna. The 3-dB axial ratio (AR) bandwidth is doubled by adding two inverted L-shaped parasitic stubs on both sides of the antenna. For validation, the antenna with the dimensions of  $0.68\lambda_0 \times 0.68\lambda_0 \times 0.044\lambda_0$  was fabricated and measured in various scenarios with an impedance bandwidth of 6.6% (5.67–6.05 GHz), an AR bandwidth of 3.85% (5.730–5.955 GHz), and a peak gain of 7.2 dBi. The measured radiation in the off-body direction is achieved with a half-power beamwidth of  $65^\circ$  and a 3-dB AR beamwidth of  $84^\circ$ . With the specified input power of 100 mW, the specific absorption rates are 0.613 and 0.294 W/kg in 1-g and 10-g average tissues. Moreover, through analysing the link budget a reliable communication can be guaranteed within 20 m in indoor line-of-sight environments.

## 1 | INTRODUCTION

With the rapid development of wireless body area networks (WBANs), wearable devices tremendously increase. The antennas integrated into wearable devices, take a critical role in wireless communications with nearby base stations. The research about wearable antennas has gradually become hotspots [1–3]. Since the wearable antenna operates within the vicinity of the human body, the loading effect of lossy tissues and structural deformation have to be taken into account in the process of antenna design [4]. In addition, owing to the motion and changeable gesture of the human body, it is difficult to keep the transceiver nodes aligned all times, causing polarization mismatch. Therefore, wearable antennas with the robust performance against the influence of human lossy body, deformation and polarization mismatch are more suitable for WBAN applications.

Various antennas have been proposed for wearable applications, such as monopole antenna [5], substrate integrated

waveguide antenna [6], and artificial magnetic conductor loaded antennas [7, 8]. However, most of the above-mentioned antennas are linearly polarized (LP), which could lead to unreliable transferring of wireless data due to the polarization mismatch caused by the human body motion and changeable gestures. Circularly polarized (CP) radiation mitigates the losses caused by polarization mismatch and multipath interference [9]. Several CP antennas including microstrip patch antennas [10–13], filtering antenna [14], and anisotropic artificial ground plane loaded antenna [15] have been investigated for wearable devices. The microstrip patch antennas [10, 11] with truncated corners are designed to generate CP unidirectional radiation. However, these antennas are fed by coaxial probes, which is inconvenient to the wearable applications. In [14], a compact CP antenna integrated with bandpass filter circuits is proposed for wearable biotelemetric devices, but it adopts a rigid substrate, which cannot conform to the human body. In [15], a flexible CP antenna etched on a polydimethylsiloxane substrate

This is an open access article under the terms of the Creative Commons Attribution License, which permits use, distribution and reproduction in any medium, provided the original work is properly cited.

© 2021 The Authors. *IET Microwaves, Antennas & Propagation* published by John Wiley & Sons Ltd on behalf of The Institution of Engineering and Technology.

at the 2.4-GHz industrial, scientific, and medical (ISM) band is studied. Nevertheless, these wearable CP antennas suffer from narrow axial ratio (AR) bandwidth, which may result in the degraded performance due to possible frequency offset.

A wearable CP antenna with a robust performance of high gain and wider AR bandwidth is investigated in the 5.8-GHz ISM band. The proposed antenna is fed by a simple microstrip line instead of a coaxial probe to avoid the protrusion. Moreover, flexible polyimide and foam material are used in this design to enhance its wearing comfort.

## 2 | ANTENNA DESIGN AND DISCUSSION

### 2.1 | Antenna design

The configuration of the proposed wearable CP antenna is depicted in Figure 1. As can be seen, the antenna is composed of three stacked layers. To be wearable and comfortable, the proposed antenna should be flexible, light weight, and adequate toughness. Hence, the top layer is a microstrip patch antenna, which is sculptured on a flexible Panasonic R-F770 substrate with a relative permittivity of  $\epsilon_r = 3.2$ , a loss tangent of  $\tan \delta = 0.002$ , and a thickness of  $h_1 = 0.12$  mm. The bottom layer is a grounded R-F770 substrate with the same thickness as the top one. Between the top and bottom layers an ethylene-vinyl acetate (EVA) foam with  $\epsilon_r = 1.17$ ,  $\tan \delta = 0.002$ , and  $h_2 = 2$  mm is filled, supporting the top layer. Two pairs of shorting pins with unequal spacing in the diagonal directions are adopted to produce two degenerated modes (DMs), achieving CP radiation [16]. Besides, a pair of inverted L-shaped parasitic stubs (ILSPSs) are loaded on both sides of the antenna, generating extra local minimum values of AR near 5.8 GHz and hence widening of the AR bandwidth. Moreover,

a pair of short slots are cut in the radiation patch to offset the equivalent inductance caused by the shorting pins, improving impedance matching. Feeding with a coaxial probe on the bottom of the antenna will cause a protrusion. In the structure of the proposed antenna, a piece of microstrip line is introduced to weld coaxial connector from the side, making the antenna more comfortable and convenient to wear. Through adjusting the structure of the proposed antenna with the aid of ANSYS HFSS v.18, the optimal values of the antenna's geometric parameters are listed in Table 1.

### 2.2 | Analysis of the CP actualization

The CP radiation is one main characteristic of the proposed antenna. To clarify the working mechanism of CP implementation, the equivalent RLC network [17] of the initial scheme is modelled to effectively describe the generation of two DMs (i.e., mode 1 ( $f_1$ ) and mode 2 ( $f_2$ )), as shown in Figure 2a. With reference to Figure 2b, it can be found that as  $\Delta d$  equals 0 mm, the antenna excites a single resonant frequency of quasi-TM<sub>10</sub>, verified in Figure 3a. Hence, only LP is

TABLE 1 Optimized antenna dimensions

Parameters	Value, mm	Parameters	Value, mm
$W_s$	35	$l_1$	5.4
$W_p$	25	$l_2$	16.5
$D$	16.6	$l_f$	5
$\Delta d$	2	$d_c$	4.1
$w_1$	0.5	$r_p$	0.5
$w_2$	1	$h_1$	0.12
$w_f$	3	$h_2$	2

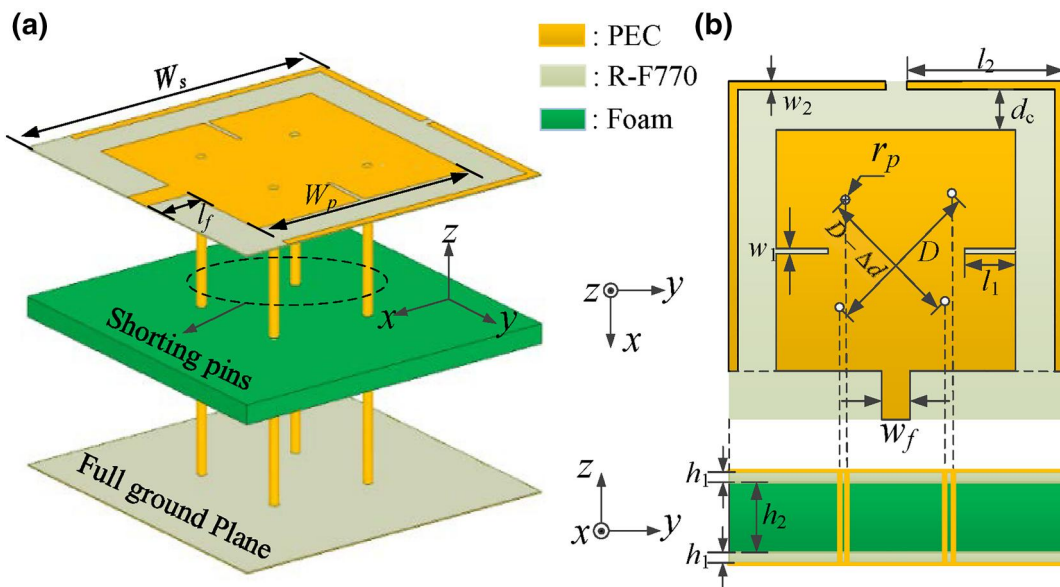
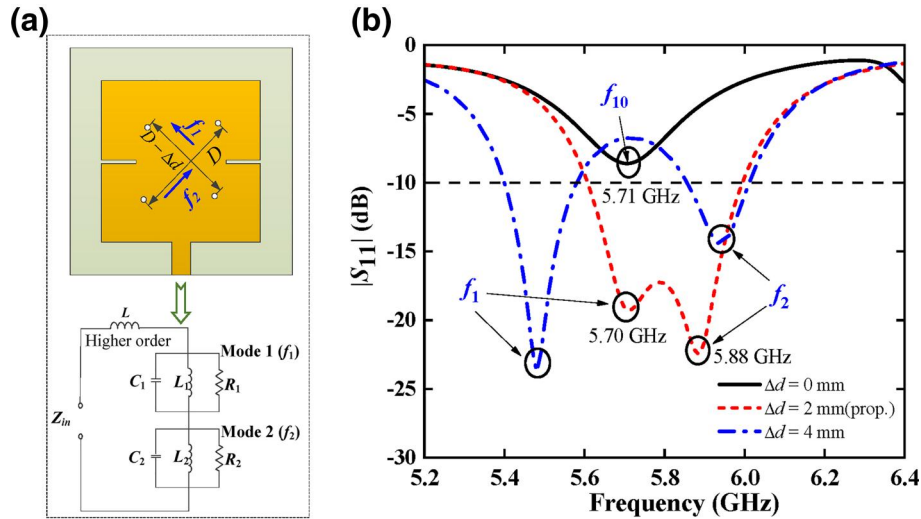


FIGURE 1 Geometry of the proposed antenna (a) Perspective view, (b) Top and side views

generated. This is mainly due to the fact that two pairs of shorting pins are symmetrical without perturbation. With  $\Delta d = 2$  mm, two resonant frequencies (i.e.  $f_1 = 5.70$  GHz and  $f_2 = 5.88$  GHz) are generated. With reference to Figure 3b, c, the directions of the current distributions at  $f_1 = 5.70$  GHz and  $f_2 = 5.88$  GHz are normal to each other. In theory, the

realization of CP should satisfy the condition that the two modes have equal amplitude and orthogonal phase. That is, left-handed CP (LHCP) or right-handed CP (RHCP) can be achieved [18] if the following conditions are satisfied.

$$|E_\phi| = |E_\theta| \quad (1)$$



**FIGURE 2** Description of the generation of two DMs (a) Equivalent electrical network modelling for the initial design with two DMs, (b) Simulated  $|S_{11}|$  for initial design under different pin offset  $\Delta d$

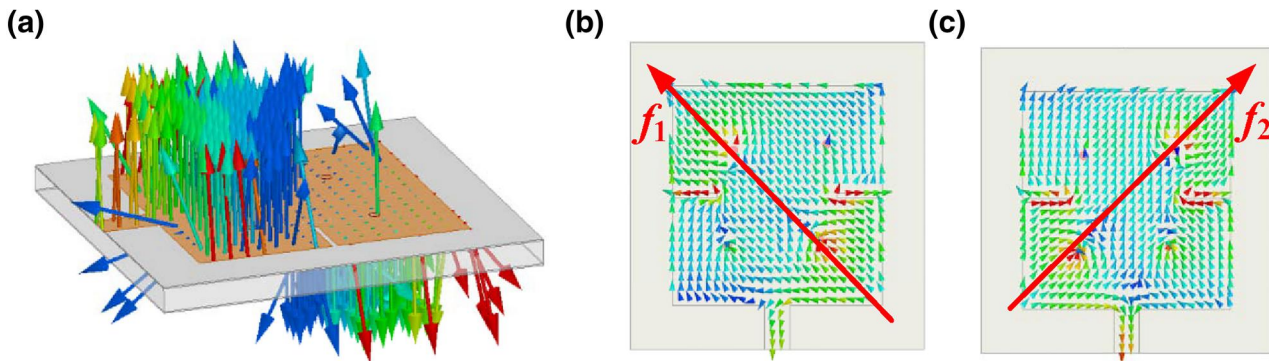


**FIGURE 3** Electric field distribution and current flow on the patch. (a) Electric field distribution at  $f_{10} = 5.71$  GHz, (b) Current flows at  $f_1 = 5.70$  GHz, and (c) Current distributions at  $f_2 = 5.88$  GHz

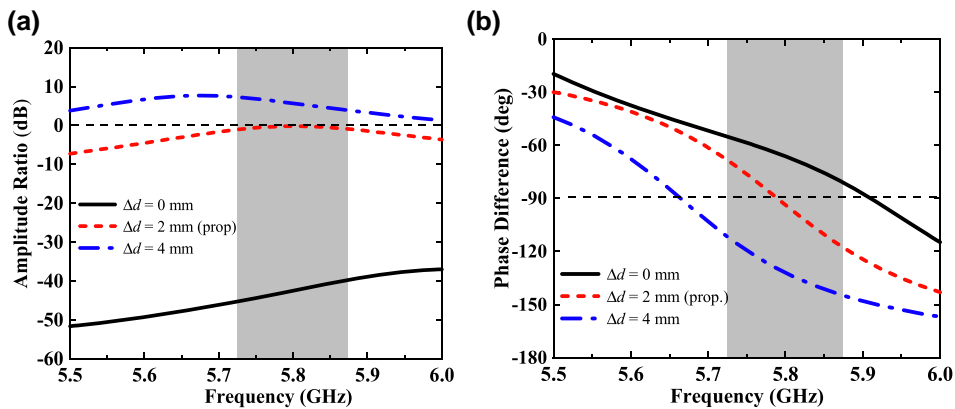


**FIGURE 4** Simulated results under different pin offset  $\Delta d$  (a) Amplitude ratios, (b) phase differences

$$\angle E_\varphi - \angle E_\theta = +90^\circ, \text{ for LHCP} \quad (2)$$

$$\angle E_\varphi - \angle E_\theta = -90^\circ, \text{ for RHCP} \quad (3)$$

The amplitude ratios ( $|E_\varphi/E_\theta|$ ) and phase differences ( $\angle E_\varphi - \angle E_\theta$ ) in the broadside direction under diverse  $\Delta d$  are computed. With reference to Figure 4a, b, it can be seen that in the case of  $\Delta d = 2$  mm, the  $|E_\varphi/E_\theta|$  and  $\angle E_\varphi - \angle E_\theta$  are closer to 0 dB and  $-90^\circ$ , respectively. Hence, according to Equations (1) and (3), a RHCP radiation is achieved.

Furthermore, the surface current distributions on the patch at 5.8 GHz are presented in Figure 5. It can be found that the composite current rotates counter-clockwise with the increasing of time by a step of  $T/4$ , demonstrating an RHCP radiation, consistent with the theoretical analysis. Similarly, LHCP radiation can be obtained. For the concise, no further explanation is carried out here.

### 2.3 | Analysis of the AR bandwidth enhancement

The proposed antenna has the wide AR bandwidth to work effectively in the harsh environment. To better understand the operating principle for broadening the AR bandwidth, the antenna topologies are evolving from Case 1 to Case 2 and the corresponding surface current distributions at 5.7–5.9 GHz are analysed in Figure 6. Compared with the current distributions

in Case 1 and Case 2 in Figure 6a,b, it can be found that the additional current component is generated on ILSPSs due to the electromagnetic coupling effect, which is the correct component needed for the circular polarization. In numerical method, the broadening of the axial ratio bandwidth is verified

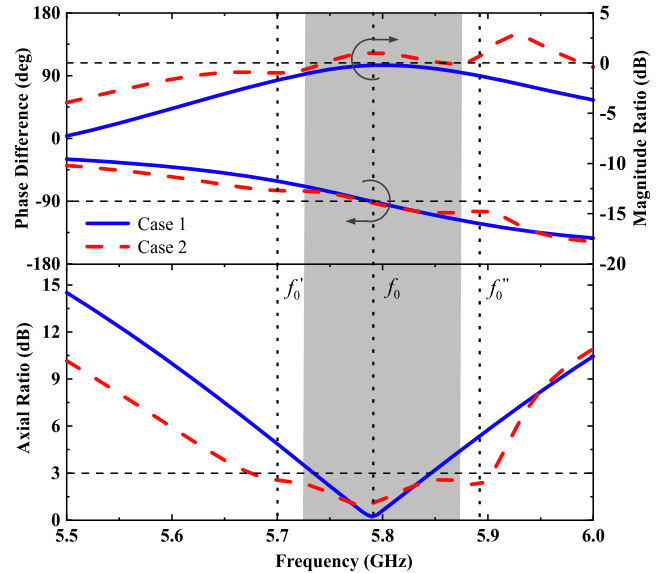


FIGURE 7 Simulated phase differences, amplitude ratios, and axial ratios in Case 1 and Case 2

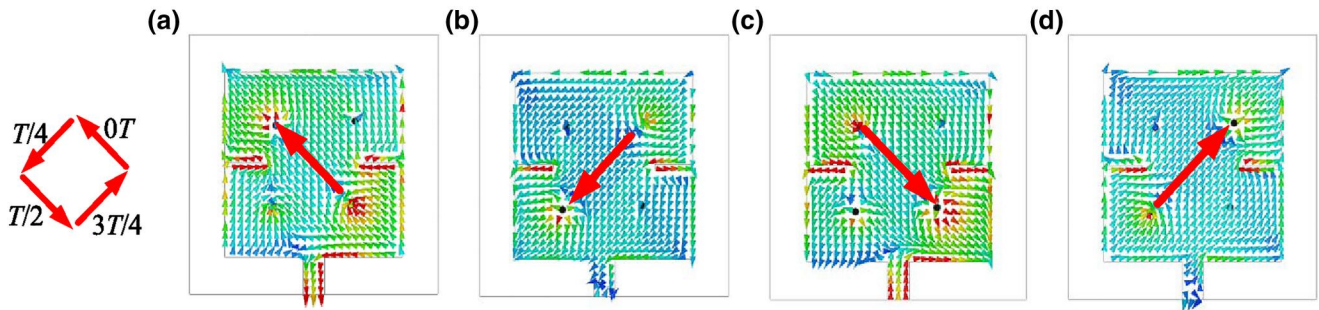


FIGURE 5 Simulated surface current distributions at 5.8 GHz (a)  $t = 0 T$ . (b)  $t = T/4$ . (c)  $t = T/2$ . (d)  $t = 3 T/4$

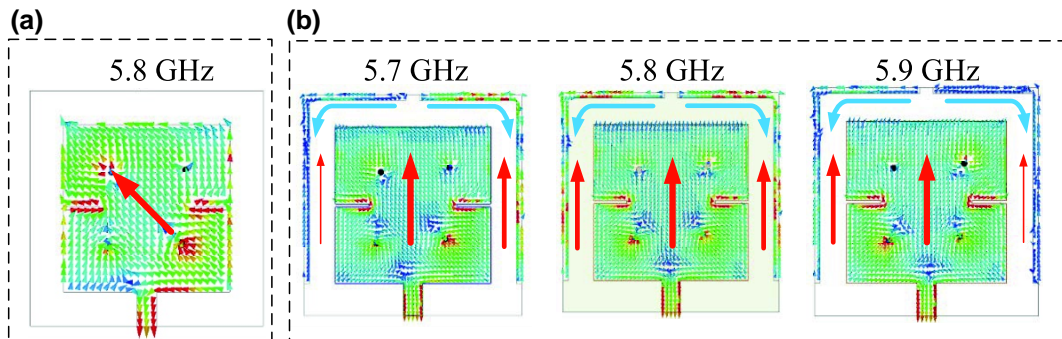


FIGURE 6 Simulated surface current distributions in different case (a) Case 1 (without ILSPS), (b) Case 2 (with ILSPS)

by computing the phase differences and amplitude ratios in Case 1 and Case 2 as presented in Figure 7.

In theory, a rectangular microstrip antenna in Case 1 is loaded with four shorting pins. Due to the inherent narrowband characteristics of microstrip patch antenna, the equal amplitude and orthogonal phase are realized only near the frequency of  $f_0$ . Hence, a single minimum AR is achieved, partially covering the 5.8-GHz ISM band. In Case 2, ILSPSs are equipped on the structure of Case 1. The amplitude ratios of closer to 0 dB and the phase differences closer to  $-90^\circ$  are realized at the frequencies of  $f_0$ ,  $f_0'$ , and  $f_0''$ , respectively. As a result, the AR reaches more than one minimum value at different frequency points, enhancing the AR bandwidth.

## 2.4 | Parametric studies

The configuration of the proposed antenna determines the performance such as impedance matching and circular polarization. Hence, all geometrical parameters are analysed. Owing to limited space, only key factors such as  $D$ ,  $l_1$ ,  $d_c$ , and  $l_2$ , are studied to identify how to influence the performance of the proposed antenna and provide design guidelines. With reference to Figure 8a, it can be found that the spacing  $D$  between

shorting pins has a tuning effect on  $|S_{11}|$  and AR. This is due to the fact that the shorting pins cause a shunt inductive effect, and adjusting the dimension of  $D$  can change the magnitude of inductance effect. Thus, it can be used to control the resonant frequency. Herein, as  $D$  is optimized to be 16.6 mm, the 5.8-GHz ISM band can be perfectly covered. As shown in Figure 8b, the length  $l_1$  of the short slot significantly affects the impedance matching of the antenna while the effect on the AR can be neglected. This is because the short slot inserted into the patch can be equivalent to the capacitance, offsetting the inductance caused by shorting pins. After optimization,  $l_1 = 5.4$  mm and  $w_1 = 0.5$  mm are given.

To illustrate how ILSPSs influence the CP bandwidth, the effects of coupling distance  $d_c$  and the length  $l_2$  of ILSPSs on  $|S_{11}|$  and AR are investigated. The width  $w_2$  of ILSPSs has little effect on antenna performance because it does not affect the current path length on ILSPSs. As shown in Figure 9a,b, the  $d_c$  and  $l_2$  greatly influence the bandwidth of the AR but slightly on its impedance bandwidth. In mechanism, this is mainly due to the fact that the  $l_2$  will change the current path on ISLPSs and  $d_c$  will affect the coupling strength between the patch and ILSPSs, both of which take an important role in the amplitude ratios and phase differences at the additional frequencies of  $f_0'$  and  $f_0''$ . After computation,  $d_c = 4.1$  mm and  $l_2 = 16.5$  mm are proposed with AR less than 3 dB at  $f_0$ ,  $f_0'$  and  $f_0''$ .

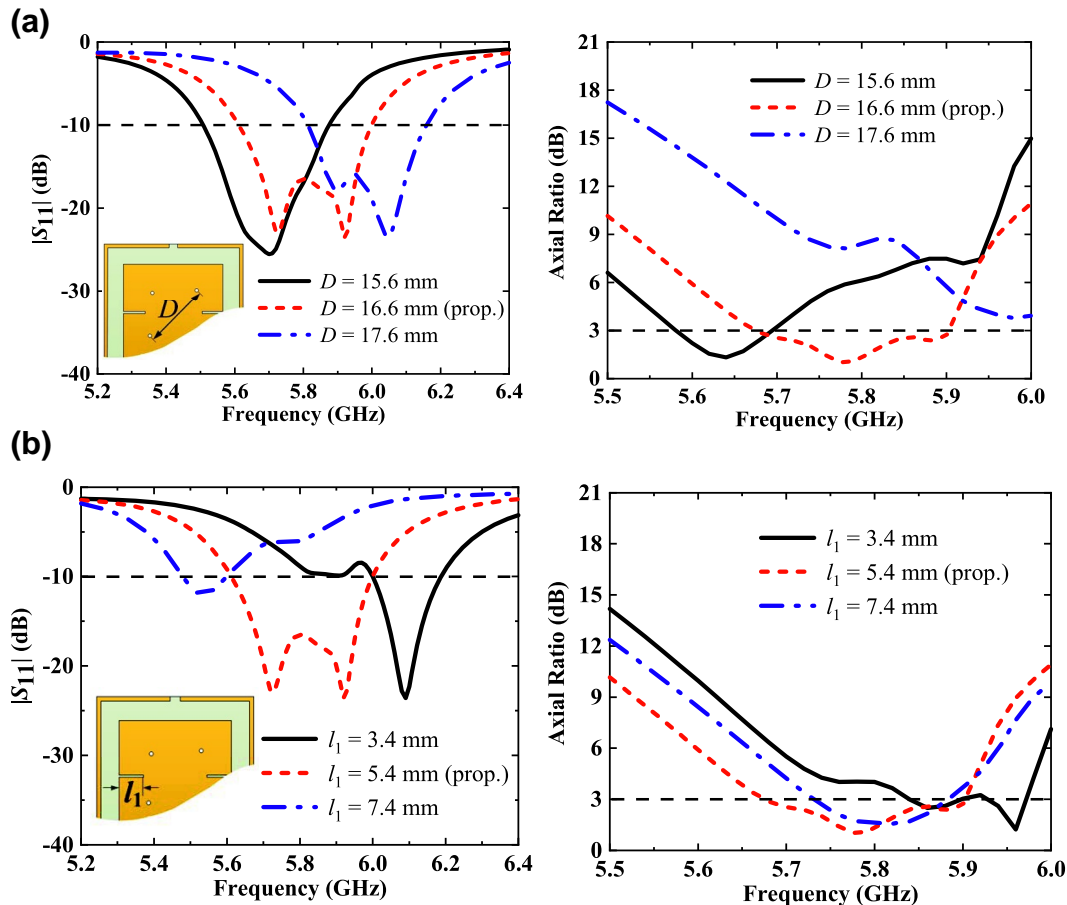


FIGURE 8 Effects of varying parameters on  $|S_{11}|$  and AR (a) Shorting pins spacing  $D$ , (b) Short slot length  $l_1$

### 3 | ANTENNA PERFORMANCE

#### 3.1 | Influence of human body

As the human tissues are lossy, dispersive, and inhomogeneous, they will affect the performance of antenna when it is worn on the body. Hence, to evaluate the effect of human tissues on the antenna performance, a multilayer phantom is constructed, as shown in Figure 10. The electrical properties at 5.8 GHz and the thickness of each tissue are given in Table 2 [19]. To save the computation time and clarify the illustration, the human model is simplified with the dimensions of  $100 \times 100$  mm, which can enable the distance between the antenna and outer

edge of the phantom greater than a quarter wavelength at the operating band.

Owing to the movement of the human body, the distance between antenna and human body would be changed. Hence, the simulated  $|S_{11}|$ , AR, and gain of the proposed

**TABLE 2** Dielectric properties and thickness of tissues at 5.8 GHz

	Skin	Fat	Muscle
$\epsilon_r$	35.114	4.955	48.485
Conductivity, S/m	3.717	0.293	4.962
Thickness, mm	$b_s = 1.3$	$b_f = 10$	$b_m = 20$

**FIGURE 9** Effects of key parameters on  $|S_{11}|$  and AR (a) Coupling distance  $d_c$ , (b) ILSPSs length  $l_2$

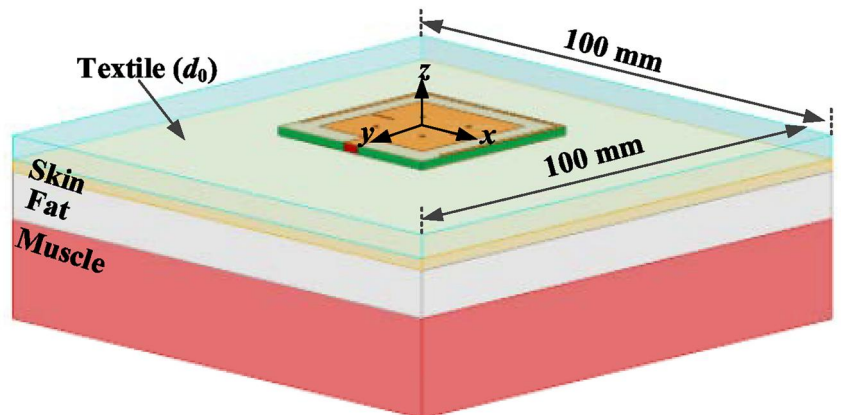
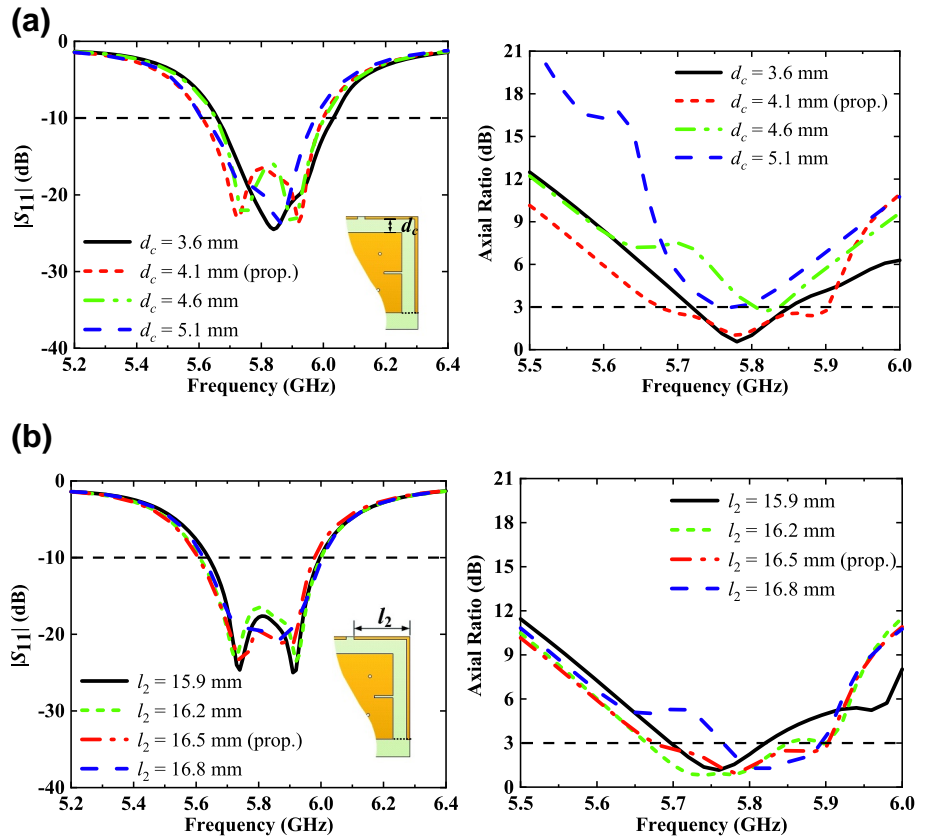


**FIGURE 10** Schematic of the multilayer human tissue model

antenna with different separation distances of  $d_0$  are studied. With reference to Figure 11a, the proposed antenna has a robust impedance matching even though there is a big fluctuation of the separation distance. As shown in Figure 11b, the AR bandwidth of the antenna is decreased as the antenna gets close to the phantom. For achieving pure CP performance and covering the required band, the optimized  $d_0$  is found to be within 2–4 mm. This gap can be guaranteed by thin clothes with different thicknesses. In addition, the gain decreases as  $d_0$  increases. Herein, to make a trade-off between the gain and AR performance, the antenna is separated from the human phantom with  $d_0 = 3$  mm. In the following experimental setup, the gap  $d_0$  was kept to the same value.

Moreover, considering that textiles are made of various materials, the effects of filling different materials between the antenna and phantom on antenna performance are studied, as shown in Figure 12a,b. The filling materials such as felt, jeans, polyester and cordura, and their dielectric properties are given in Table 3 [20]. It can be found that different textiles only cause slight variations in resonance frequency, AR and gain. This is mainly due to the fact that the antenna has a complete ground plane, which mitigates the impact of textiles on the antenna performance.

Furthermore, due to the fact that the thickness of each tissue in different parts of the human body is different, especially the thicknesses of fat and muscle, it is necessary to study the influence of tissue thickness variation on antenna performance. As observed in Figure 13a,b, the changes in the thicknesses of fat and muscle of the phantom do not affect the

antenna performance, indicating that the proposed antenna can work on any part of the human body.

### 3.2 | Robustness to structural deformation

As the shape of human body is not flat, and even different parts have different curvatures, it will be comfortable for the wearable antenna to be flexible and conformal to the human body. To evaluate the performance of the proposed antenna under structural deformation, as shown in Figure 14, the proposed antenna is conformed to the human model with three different bending radii, representing the wrist, upper arm, and thigh. Without losing generality, the felt material with  $h_3 = 3$  mm is filled between the antenna and human model, imitating clothes. As illustrated in Figure 15a, the resonant frequency shifts up slightly as the proposed antenna is curved. This is because the proposed antenna bends along the current direction on the patch, which reduces the effective length of the current path [21], and then causes the resonant frequency shifts up. Also, the impedance matching is deteriorated slightly at 5.7 GHz due to the change of current path. Anyhow, the  $-10$ -dB bandwidth ranges from 5.64 to 6.01 GHz, fully

TABLE 3 Dielectric properties of each textile

	Felt	Jeans	Polyester	Cordura
$\epsilon_r$	1.45	1.6	1.9	1.9
$\tan \delta$	0.02	0.04	0.0045	0.0098

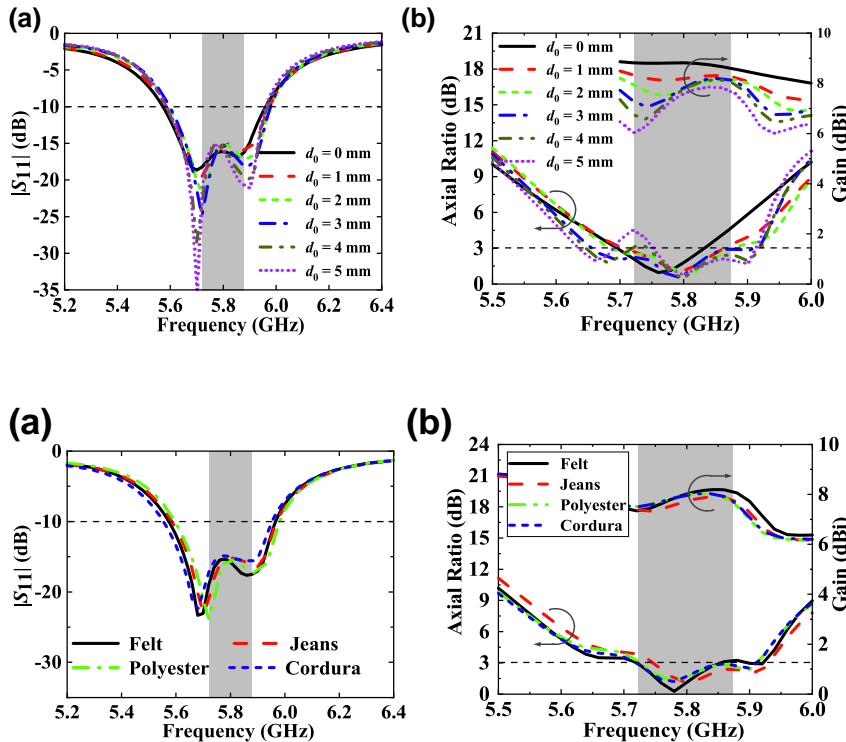
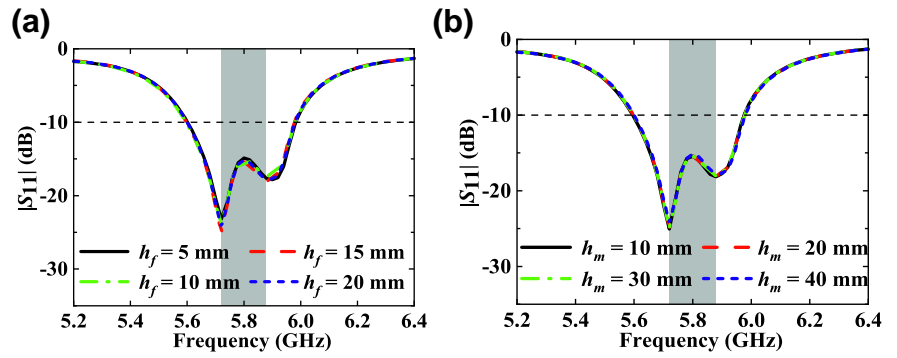


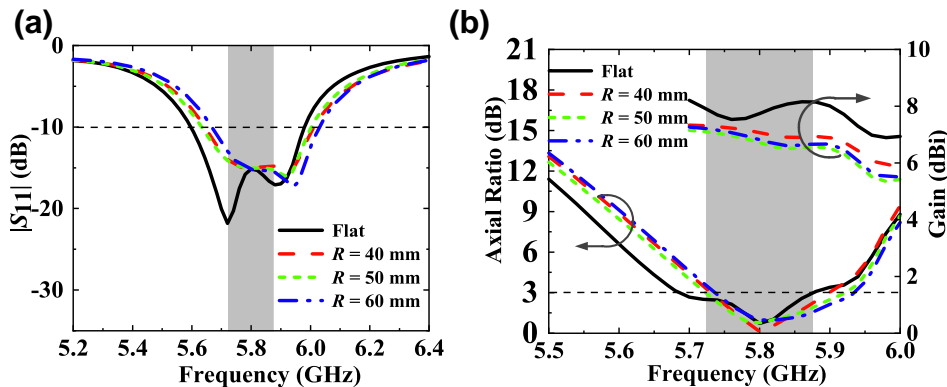
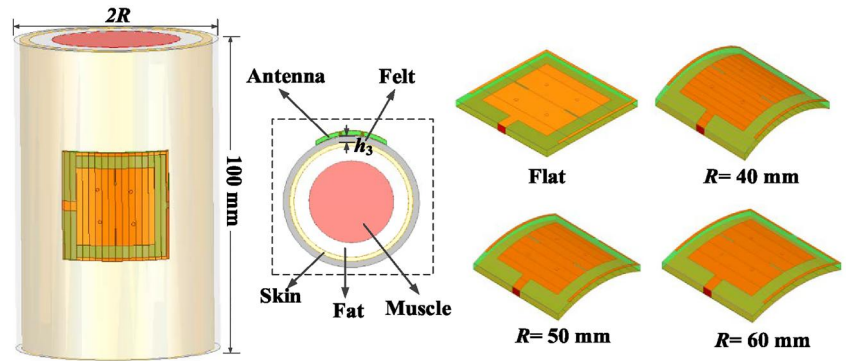
FIGURE 11 Simulated results of the proposed antenna in different separation distances ( $d_0$ ) between the antenna and the multilayer tissue model (a)  $|S_{11}|$ , (b) AR and gain

FIGURE 12 Effects of different textile materials on  $|S_{11}|$ , AR and gain (a)  $|S_{11}|$ , (b) AR and gain

**FIGURE 13** Effects of tissue thickness on antenna  $|S_{11}|$  (a) Fat thickness  $h_f$ , (b) Muscle thickness  $h_m$



**FIGURE 14** Cylindrical phantom and the bended antenna on the phantom with different bending radii



**FIGURE 15** Simulated results of the proposed antenna in different bending radii (a)  $|S_{11}|$ , (b) AR and gain

covering the 5.8-GHz ISM band. In addition, the simulated AR and gain of the proposed antenna for all the cases are presented in Figure 15b. It can be observed that the performance of CP has good purity in the operating band while the gain is deteriorated a little as the antenna is curved. The reason for the lower gain may also be caused by the shrinkage of the effective size of the antenna. However, in any condition the performance is merit, making the proposed antenna suitable for wearable device.

### 3.3 | Consistency on the Hugo voxel model

The above-mentioned simulated results are obtained on the multilayer phantom. To approximate closely to the real human

body, the Hugo voxel model is introduced in the CST Microwave Suite to study the radiation performance and specific absorption rates (SAR) of the proposed antenna. As shown in Figure 16, the proposed antenna is mounted about 3 mm high above the right upper arm of the human model with a radius of  $R = 50$  mm. The simulated results, such as  $|S_{11}|$ , AR and gain, are compared with those obtained in HFSS (from Figures 14 and 15 with  $R = 50$  mm). It is illustrated in Figure 17 that those results in both electromagnetic softwares agree well with each other. Besides, the simulated normalized radiation patterns at 5.8 GHz are plotted in Figure 18. It can be seen that RHCP is achieved with a good cross-polarization ratio of more than 20 dB in the broadside direction. Meanwhile, the FBR is more than 18 dB, achieving low backward radiation.

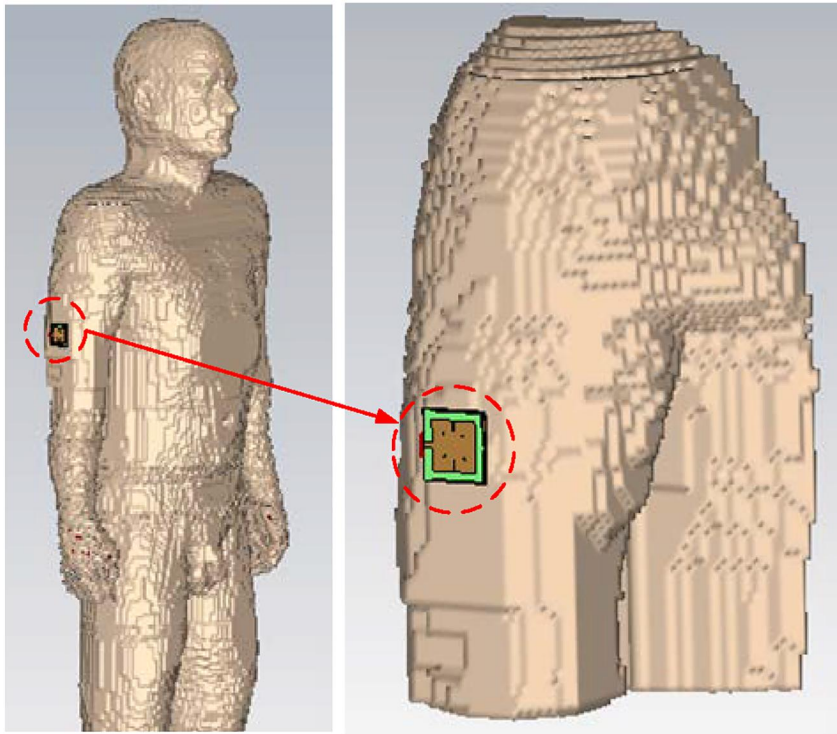


FIGURE 16 Simulation setup for the proposed antenna on the Hugo voxel model in CST

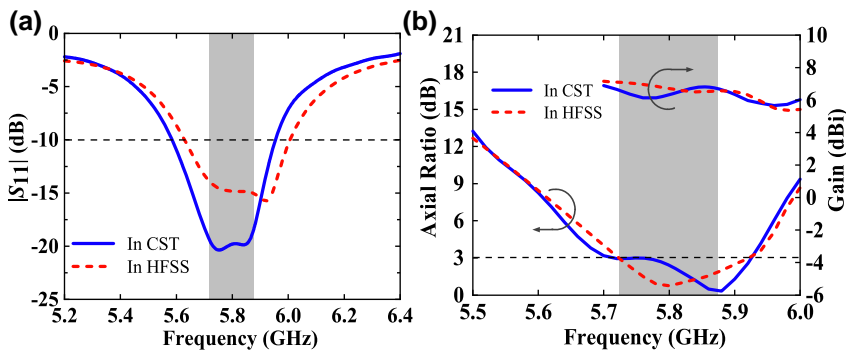


FIGURE 17 Simulated results of the proposed antenna in CST and HFSS (a)  $|S_{11}|$ , (b) AR and gain

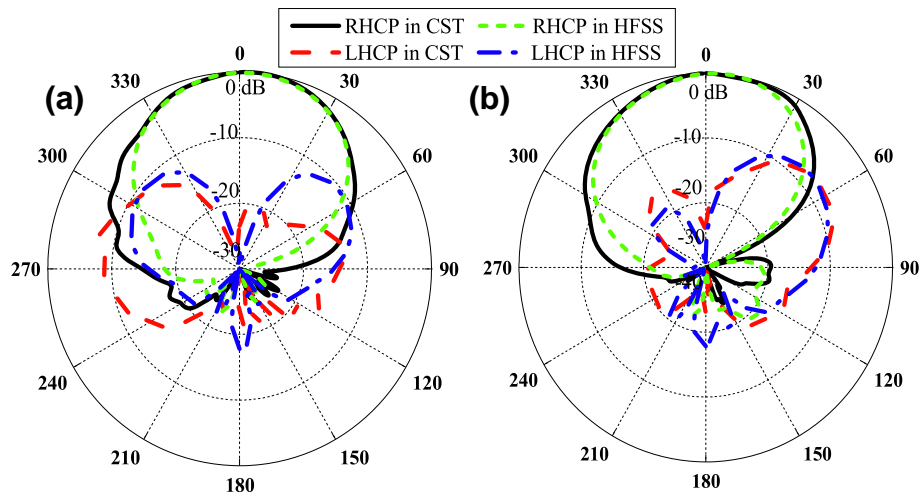


FIGURE 18 Normalized radiation patterns of the proposed antenna at 5.8 GHz in different electromagnetic software (a)  $xz$ -plane, (b)  $yz$ -plane

Besides, due to the existence of distance difference  $\Delta d$ , the geometry of the proposed antenna is non-symmetrical with the  $xz$ - and  $yz$ -planes, leading to the tilted radiation pattern in Figure 18b.

To ensure that the antenna is harmless to human health, the absorbed radiofrequency energy of the proposed antenna by human tissues must be no more than critical values, that is, the SAR should be less than 1.6 W/kg averaged over 1-g tissue of American threshold or 2 W/kg averaged over 10-g tissue of European threshold, according to the specification in the IEEE C95.1 standard [22]. The SAR can be calculated through the following equation:

$$SAR = \frac{\sigma |E|^2}{\rho} \quad (4)$$

where  $\sigma$  represents the conductivity of the tissue in S/m,  $E$  denotes the effective electric field in V/m, and  $\rho$  is the density in  $kg/m^3$ . As a benchmark, the input power accepted by the antenna for evaluating SAR performance is set to 100 mW. The computed SAR distribution on the Hugo model at 5.8 GHz is

plotted in Figure 19. As can be seen, the maximum SAR is 0.613 W/Kg under the mass of 1 g and 0.294 W/Kg under 10 g mass on average, respectively, both of which are lower than the limitation defined by IEEE C95.1 standard.

#### 4 | MEASUREMENT RESULTS AND DISCUSSION

To validate the theoretical design and simulated results, a proof-of-concept prototype was fabricated. The measurement setup was built as demonstrated in Figure 20. A male volunteer (1.70 m in height and 62 kg in weight) was involved. The reflection coefficient was measured by Agilent N5230A vector network analyser, as shown in Figure 20a. For the electrical properties of the pork are similar to those of human body and also the pork is cheap and is easy to get it, the pork is used to work as phantom in the experiment. The dimensions of the fresh pork are about  $103 \times 103 \times 32$  mm, which are approximate to those of the numerical phantom. The far-field radiation characteristics of the prototype were tested on the fresh pork in anechoic chamber, as presented in Figure 20b.

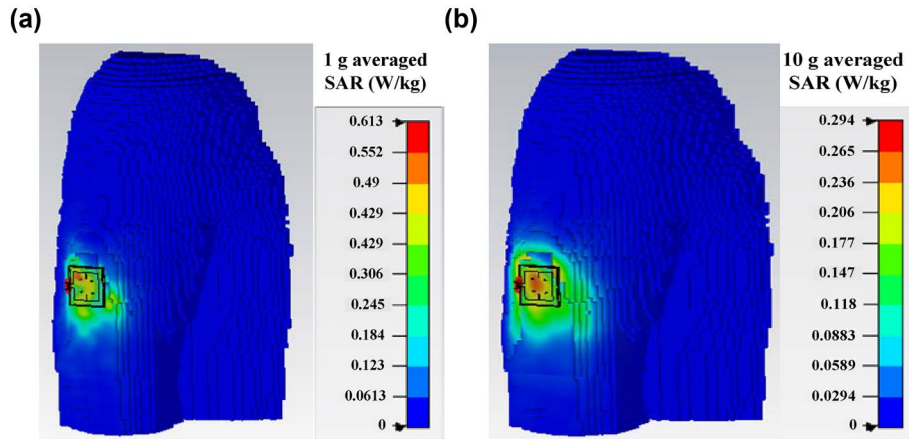


FIGURE 19 Simulated SAR on the Hugo voxel model at 5.8 GHz (a) 1-g tissue, (b) 10-g tissue

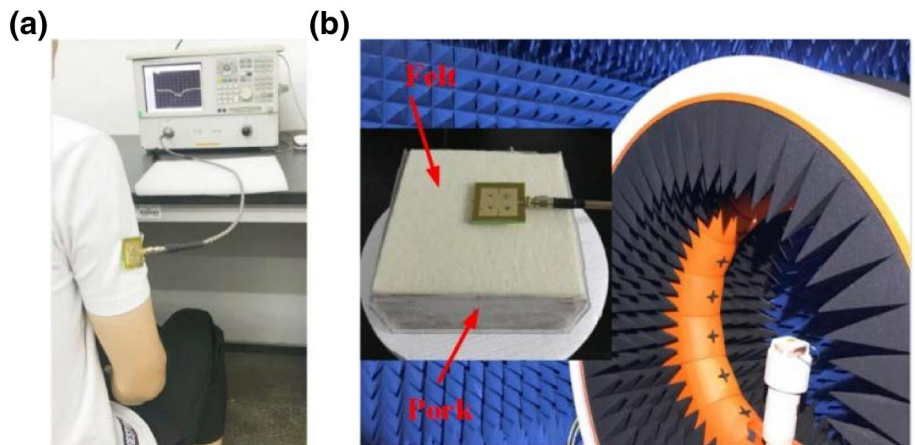


FIGURE 20 Measurement settings for the proposed antenna (a)  $|S_{11}|$  on human body, (b) Measurement setup in the Satimo Starlab anechoic chamber

## 4.1 | Measurement results

The simulated and measured  $|S_{11}|$  of the proposed antenna in free space and on phantom is compared, as illustrated in Figure 21. The measured impedance bandwidth for  $|S_{11}| < -10$  dB in the free space ranges from 5.66 to 6.06 GHz (6.8%). When the proposed antenna was measured on pork, different textile material, including felt, jeans, polyester and cordura, was filled between the proposed antenna and pork to verify that clothing material has slight effect on the antenna performance. As expected, the measurement results are consistent in all scenarios. On average, the measured impedance bandwidth on pork ranges from 5.67 to 6.05 GHz (6.6%). Notably, compared with the simulated results, the measured ones are shifted up to about 40 MHz due to the deviation caused by the fabrication errors and the possible air gap between the R-F770 substrate and EVA foam. Moreover, the  $|S_{11}|$  of the proposed antenna was measured on the different parts of human body, including wrist, upper arm, and thigh, as shown in Figure 22. As can be seen, the impedance characteristics match well and almost remain

unchanged in all scenarios, which verifies the conclusion that different parts of the human body have little influence on the antenna performance in numerical simulation.

In Figure 23, the measured AR and gain of the proposed antenna are compared with the simulated ones. The measured 3-dB AR bandwidth on pork is covered from 5.730 to 5.955 GHz (3.85%). The measured peak gain is about 7.2 dBi in the 5.8-GHz ISM band, which is 1.2 dBi lower than the peak gain in free space. This is due to the fact that the power is dissipated by the human tissues as the antenna is in proximity to human body. In addition, as illustrated in Figure 24, the measured 3-dB AR beamwidths in free space and on pork are  $91^\circ$  and  $84^\circ$ , respectively. Furthermore, the simulated and measured normalized radiation patterns at 5.8 GHz are illustrated in Figure 25. It can be observed that RHCP is the principal polarization in the operating frequency band with an insignificant back lobe. Also, the measured half-power beamwidths in the two planes are  $65^\circ$  and  $78^\circ$ , respectively. The divergence between the simulated and measured radiation patterns is mainly attributed to the difference between numerical phantom and pork trunk.

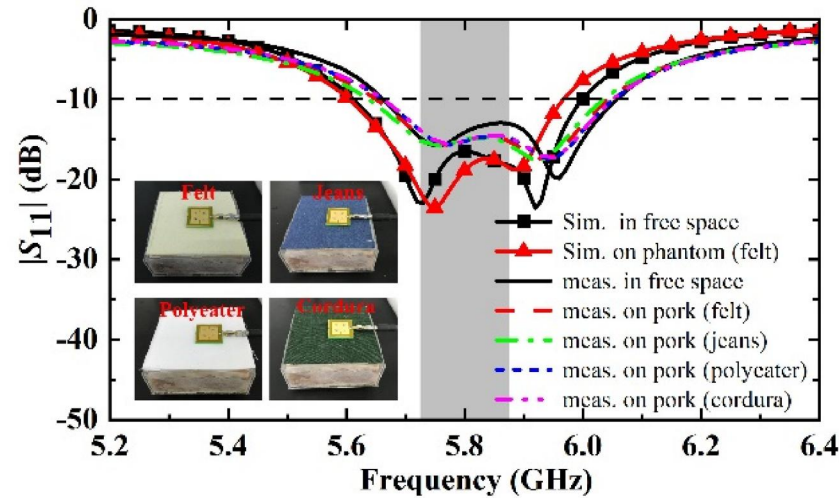


FIGURE 21 Simulated and measured  $|S_{11}|$  of the proposed antenna in different scenarios

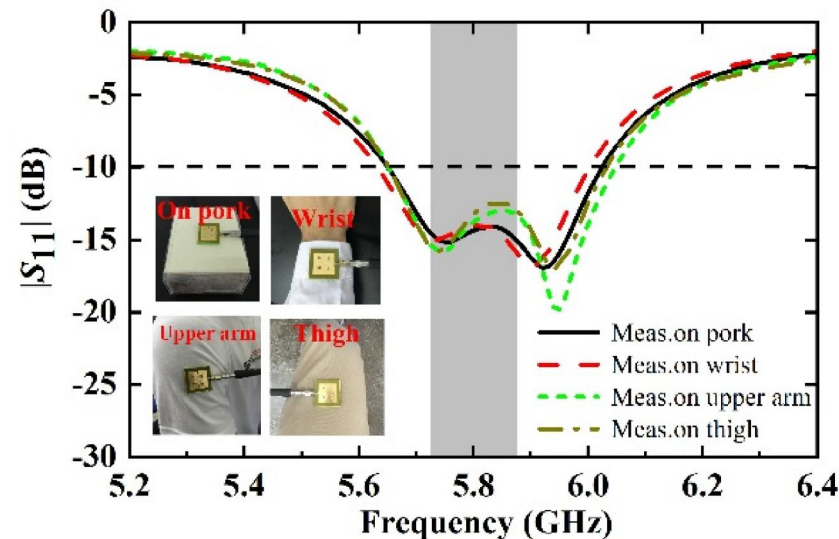


FIGURE 22 Measured  $|S_{11}|$  of the proposed antenna on pork and on different parts of human body

## 4.2 | Link budget analysis

To evaluate the communication ability between the proposed antenna and an external receiver near the body, the communication link budget is investigated. Assuming a good

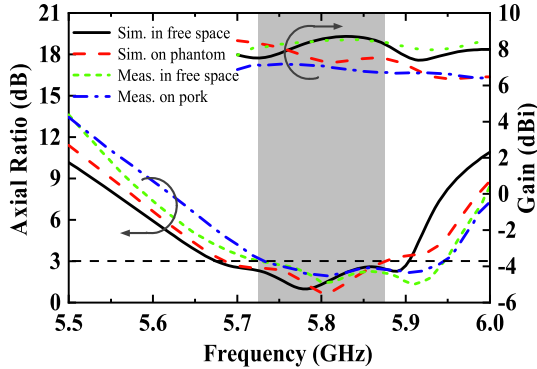


FIGURE 23 Simulated and measured AR and gain of the proposed antenna in free space and on the phantom

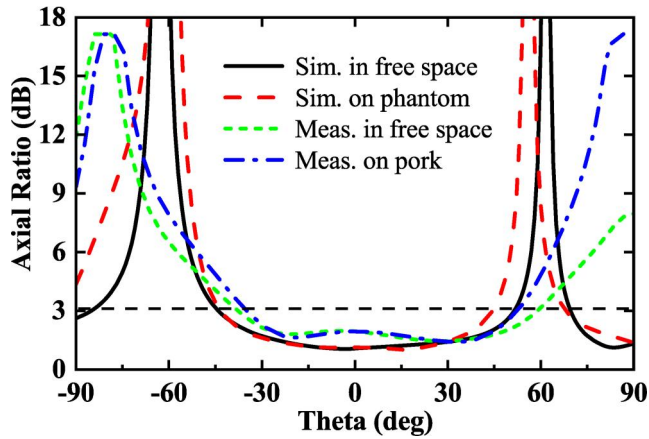


FIGURE 24 Simulated and measured AR beamwidths of the proposed antenna in free space and on the phantom at 5.8 GHz

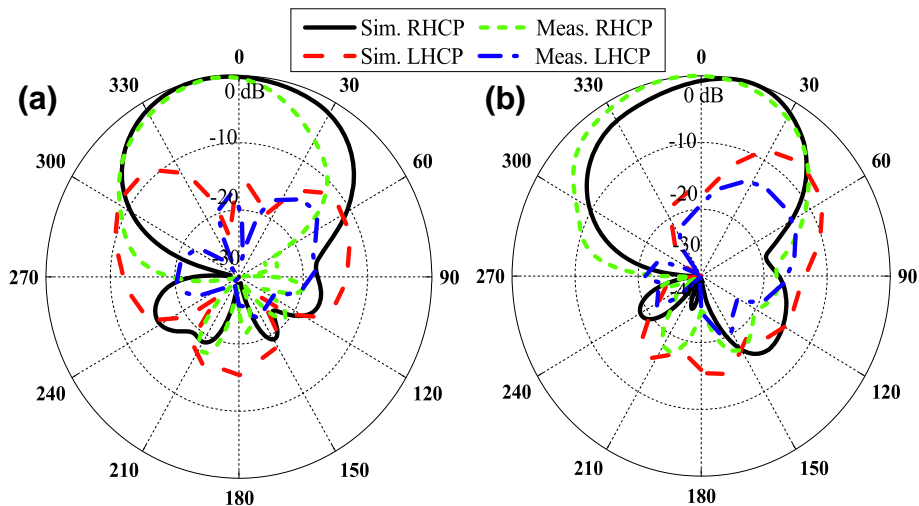


FIGURE 25 Simulated and measured normalized radiation patterns of the proposed antenna on phantom at 5.8 GHz (a)  $xz$ -plane, (b)  $yz$ -plane

impedance matching, the Friis power transmission formula can be written as [23].

$$P_r[\text{dBm}] = P_t[\text{dBm}] + G_t[\text{dB}] - \text{PL}_{\text{dB}}(d) + G_r[\text{dB}] \quad (5)$$

with multipath propagation environment

$$\text{PL}_{\text{dB}}(d) = 10n \log\left(\frac{d}{d_r}\right) + 20 \log\left(\frac{4\pi d_r}{\lambda}\right) + \chi_\sigma \quad (6)$$

where  $P_r$  and  $P_t$  represent the received ( $Rx$ ) and transmitted ( $Tx$ ) power, respectively;  $G_r$  and  $G_t$  are the gains of the corresponding  $Rx$  and  $Tx$  antennas;  $\lambda$  is the wavelength in free space, and  $d$  is the distance between  $Rx$  and  $Tx$  antennas;  $d_r$  is the reference distance (set to be 1 m);  $\chi_\sigma$  is the shadowing factor for normal distribution with a standard deviation  $\sigma$ , and  $n$  represents the path-loss exponent decided by the different propagation scenarios, such as free space ( $n = 2$ ), indoor line-of-sight (LOS) path ( $n = 1.5$ ), for example, corridors, and indoor non-line-of-sight (NLOS) path ( $n = 3$ ), for example, dense furnished rooms.

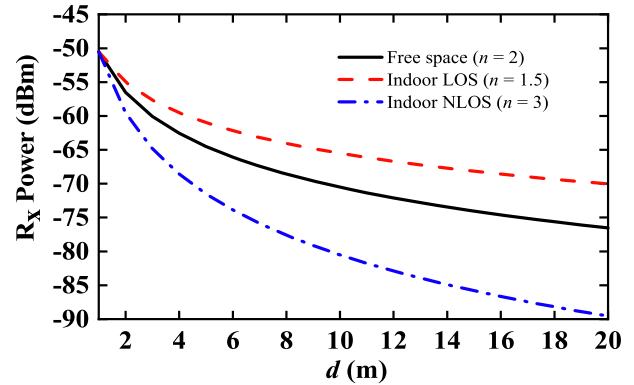


FIGURE 26 Calculated  $Rx$  power for three scenarios at 5.8 GHz

**TABLE 4** Comparison of the proposed antenna with other designs

Ref.	$f_0$ , GHz	Bandwidth		Peak Gain, dBi	Type of Antenna	Feed Method	Dimensions, $\lambda_0 \times \lambda_0 \times \lambda_0$
		$ S_{11}  < -10$ dB	AR < 3 dB				
[1]	5.5	17.3%	LP	6.7	Flexible	Probe	$0.77 \times 0.51 \times 0.073$
[6]	5.8	4.0%	LP	3.12	Flexible	Microstrip	$1.45 \times 0.81 \times 0.019$
[7]	2.45	5.7%	LP	6.88	Semi-flexible	Microstrip	$0.56 \times 0.56 \times 0.013$
[8]	2.4	5.5%	LP	6.2	Semi-flexible	Microstrip	$0.49 \times 0.34 \times 0.028$
[10]	2.45	8.9%	2.27%	6.03	Flexible	Probe	$0.82 \times 0.82 \times 0.032$
[11]	2.4	4.1%	1.25%	5.7	Flexible	Probe	$0.44 \times 0.44 \times 0.013$
[12]	2.45	6.4%	1.63%	2.25	Flexible	Microstrip	$0.74 \times 0.74 \times 0.008$
[13]	2.4	12.7%	2.91%	4.4	Flexible	Microstrip	$0.97 \times 0.97 \times 0.03$
[14]	2.4	4.5%	2.40%	3.5	Rigid	Probe	$0.44 \times 0.44 \times 0.045$
[15]	2.4	10.5%	2.72%	5.2	Flexible	Microstrip	$0.41 \times 0.41 \times 0.045$
Prop.	5.8	6.6%	3.85%	7.2	Flexible	Microstrip	$0.68 \times 0.68 \times 0.044$

An external CP dipole antenna with a gain of  $G_r = 2.15$  dBi is introduced to work as the receiver, and the input power is set to  $P_t = -10$  dBm. The  $R_x$  received power ( $P_r$ ) can be calculated using Equations (5) and (6). As shown in Figure 26, the  $P_r$  of the NLOS link is lower than that of the LOS link at 5.8 GHz. This is mainly because the obstacles in NLOS environment cause electromagnetic waves to be decayed more. Assuming that the minimum receiver sensitivity is  $-70$  dBm for 5.8-GHz ISM band applications [24], a reliable communication link can be guaranteed within 20 m in indoor LOS environments.

### 4.3 | Performance comparison

The performances of the proposed antenna and previously reported wearable antennas are compared in Table 4, wherein,  $\lambda_0$  denotes the wavelength of the operating frequency in free space. It can be observed that the antennas in [1, 6–8] are LP, which could lead to unreliable transferring of wireless data due to the polarization mismatch caused by the human body motion and changeable gestures. In [10, 11, 14], although these antennas achieve CP radiation, they are fed by a probe, making them inconvenient to wear. Compared with the reported antennas, the proposed antenna has the advantages of conformability, CP, wider AR bandwidth, and higher gain.

## 5 | CONCLUSION

A flexible CP antenna operating in 5.8-GHz ISM band has been presented. The proposed antenna achieves wider AR bandwidth by adding two ILSPs on both sides of the antenna. Due to the adoption of the fully flexible material, the antenna is conformal to the curve-shaped human body, being worn comfortably. In addition, human body loading and structural deformation are thoroughly analysed, which shows the strong

robustness of the antenna. Moreover, the effect of different wearable material is considered, illustrating that the performance of the proposed antenna is immune to the influence of clothes. To verify the numerical design, the prototype was fabricated. When measured on the fresh pork, the impedance and AR bandwidths are 6.6% and 3.85%, respectively, fully covering the 5.8 GHz ISM band with a peak gain of 7.2 dBi. Moreover, through wearable safety evaluation and link budget analysis, it is assured that the proposed antenna meets the health safety requirements, and a reliable communication with the outside receiver can be realized within a range of 20 m in an indoor LOS environment. These merited properties of the proposed antenna make it a potential candidate for the off-body communications in WBAN systems.

### ORCID

Hong Cai Yang  <https://orcid.org/0000-0003-4353-3950>

### REFERENCES

- Gao, G.P., et al.: A wearable PIFA with an all-textile metasurface for 5 GHz WBAN applications. *IEEE Antennas Wirel. Propag. Lett.* 18, 288–292 (2019)
- Poffelie, L.A.Y., et al.: A high-fidelity all-textile UWB antenna with low back radiation for off-body WBAN applications. *IEEE Trans. Antennas Propag.* 64(2), 757–760 (2016)
- Liu, X.Y., et al.: A planar windmill-like broadband antenna equipped with artificial magnetic conductor for off-body communications. *IEEE Antennas Wirel. Propag. Lett.* 15, 64–67 (2016)
- Hall, P.S., Hao, Y.: *Antennas and Propagation for Body-Centric Wireless Communications*, 2nd ed. Artech House, USA (2012)
- Suma, M.N., Bybi, P.C., Mohanan, P.: A wideband printed monopole antenna for 2.45 GHz WLAN applications. *Microw. Opt. Technol. Lett.* 48(5), 871–873 (2006)
- Hong, Y., Tak, J., Choi, J.: An all-textile SIW cavity-backed circular ring-slot antenna for WBAN applications. *IEEE Antennas Wirel. Propag. Lett.* 15, 1995–1999 (2016)
- Abbasi, M.A.B., et al.: Compact EBG-backed planar monopole for BAN wearable applications. *IEEE Trans. Antennas Propag.* 65(2), 453–462 (2017)

8. Jiang, Z.H., et al.: A compact, low-profile metasurface-enabled antenna for wearable medical body-area network devices. *IEEE Trans. Antennas Propag.* 62(8), 4021–4030 (2014)
9. Lui, K.W., Murphy, O.H., Toumazou, C.: A wearable wideband circularly polarized textile antenna for effective power transmission on a wirelessly-powered sensor platform. *IEEE Trans. Antennas Propag.* 61(7), 3873–3876 (2013)
10. Hertleer, C., et al.: A textile antenna for off-body communication integrated into protective clothing for firefighters. *IEEE Trans. Antennas Propag.* 57(4), 919–925 (2009)
11. Ismail, M.F., et al.: Compact circularly polarized textile antenna', *Proc. IEEE Symp. Wireless Tech. Appl.*, Kota Kinabalu, Malaysia pp. 134–136. (Oct. 2014)
12. Rizwan, M., Rahmat-Samii, Y., Ukkonen, L.: Circularly polarized textile antenna for 2.45 GHz. In: *Proc. International Microwave Workshop Series on RF and Wireless Technologies for Biomedical and Healthcare Applications*, TaiPei, Taiwan, pp. 21–22 (2015)
13. Locher, I., et al.: Design and characterization of purely textile patch antennas. *IEEE Trans. Adv. Packag.* 29(4), 777–788 (2006)
14. Jiang, Z.H., Gregory, M.D., Werner, D.H.: Design and experimental investigation of a compact circularly polarized integrated filtering antenna for wearable biotelemetric devices. *IEEE Trans. Biomed. Circuits Syst.* 10(2), 328–338 (2016)
15. Jiang, Z.H., et al.: Compact, highly efficient, and fully flexible circularly polarized antenna enabled by silver nanowires for wireless body-area networks. *IEEE Trans. Biomed. Circuits Syst.* 11(4), 920–932 (2017)
16. Zhang, X., Zhu, L.: High-gain circularly polarized microstrip patch antenna with loading of shorting pins. *IEEE Trans. Antennas Propag.* 64(6), 2172–2178 (2016)
17. Garg, R., et al.: *Microstrip Antenna Design Handbook*. Artech House, Norwood, MA, USA (2001)
18. Lin, Y.F., et al.: Proximity-fed circularly polarized slotted patch antenna for RFID handheld reader. *IEEE Trans. Antennas Propag.* 61(10), 5283–5286 (2013)
19. Zhu, X.Q., Guo, Y.X., Wu, W.: Miniaturized dual-band and dual-polarized antenna for MBAN applications. *IEEE Trans. Antennas Propag.* 62(7), 2805–2814 (2016)
20. Rita, S., et al.: Textile materials for the design of wearable antennas: a survey. *Sensors*. 12, 15841–15857 (2012)
21. Ling, N.S., Yahya, R.: A systematic investigation of rectangular patch antenna bending effects for wearable applications. *IEEE Trans. Antennas Propag.* 66(5), 2219–2228 (2018)
22. IEEE Standard C95.1–2005: IEEE standard for safety levels with respect to human exposure to radiofrequency electromagnetic fields, 3 kHz to 300 GHz, vol. 3. (2006)
23. Kiourti, A., Nikita, K.S.: Miniature scalp-implantable antennas for telemetry in the MICS and ISM bands: design, safety considerations and link budget analysis. *IEEE Trans. Antennas Propag.* 60(8), 3568–3575 (2012)
24. Porcino, D., Hirt, W.: Ultra-wideband radio technology: potential and challenges ahead. *IEEE Commun. Mag.* 41(7), 66–74 (2003)

**How to cite this article:** Yang HC, Liu XY, Fan Y, Tentzeris MM. Flexible circularly polarized antenna with axial ratio bandwidth enhancement for off-body communications. *IET Microw. Antennas Propag.* 2021;15:754–767. <https://doi.org/10.1049/mia2.12081>